RESEARCH ARTICLE

Multiphysics CFD and Electrochemical Assessment of Silicon Carbide (SiC) Heat Exchangers for Corrosive Waste-heat Recovery in Process Industries

Samuel Oliver Effiom[1,*], **Maria Kaka Etete Enoh**[1], **Ukeme Enoh Akpan**[1], **Precious-Chibuzo Effiom**[2] and **Fidelis Ibiang Abam**[2]

[1] Department of Mechanical Engineering, University of Cross River State, Calabar 540281, Nigeria
[2] Faculty of Engineering and Technology, University of Calabar, Calabar 540271, Nigeria

Abstract

Corrosive waste-heat recovery systems suffer material degradation, performance loss and high maintenance when conventional metallic heat exchangers face chloride-, carbonate- and sulfur-bearing condensates. This study presents a multiphysics CFD-electrochemical assessment of silicon carbide (SiC) for heat exchangers, via a 3D shell-and-tube model in COMSOL Multiphysics coupling turbulent flow, conjugate heat transfer, species transport and electrochemical corrosion. The thermal model considered high-pressure ammonia (tube side) and pressurized water (shell side); the corrosion model represented a flue-gas condensate/electrolyte containing Cl^-, NH_4^+, HCO_3^-, CO_3^{2-}, HSO_3^-/SO_4^{2-} and NO_3^- at the wetted surface, with electrochemical behavior resolved via secondary/tertiary current-distribution (Nernst–Planck/Butler–Volmer) formulations. Base-case results gave heat-transfer coefficients of 620 vs. 420 W m^{-2} K^{-1} (47.6% improvement), a pressure-drop reduction from 2.63 to 1.92 Pa, and a thermal–hydraulic performance factor of 1.64 (SiC vs. stainless steel). Electrochemical simulations predicted lower localized current density and corrosion flux for SiC than stainless steel under the same electrolyte chemistry, though as model-based comparative indicators rather than validated corrosion rates. Sensitivity screening showed SiC thermal conductivity, wall roughness, electrolyte conductivity and chloride concentration affect the magnitude of improvement, though the base-case trend remained favorable. The study offers a verified, literature-benchmarked framework for preliminary material screening, identifying experimental corrosion testing, temperature-dependent properties and thermo-electrochemical coupling as next steps before industrial adoption.

Keywords: Silicon carbide, CFD, electrochemical corrosion, waste-heat recovery, shell-and-tube heat exchanger, Nernst–Planck transport.

Submitted: 14 May 2026
Accepted: 11 June 2026
Published: 16 June 2026

Vol. 2, **No.** 2, 2026.
10.62762/IJTSSE.2026.236790

***Corresponding author:**
✉ Samuel Oliver Effiom
samueloliver@unicross.edu.ng

Citation
Effiom, S. O., Enoh, M. K. E., Akpan, U. E., Effiom, P. C., & Abam, F. I. (2026). Multiphysics CFD and Electrochemical Assessment of Silicon Carbide (SiC) Heat Exchangers for Corrosive Waste-heat Recovery in Process Industries. *International Journal of Thermo-Fluid Systems and Sustainable Energy*, 2(2), 81–100.

1 Introduction

Improving energy efficiency and reducing avoidable thermal losses remain central priorities in chemical and process industries because energy costs, carbon-management requirements and equipment reliability are now linked directly to plant profitability [1–6]. Industrial waste heat is discharged through exhaust gases, cooling streams, reactor effluents and refrigeration loops. Recovering part of this heat can reduce fuel consumption and emissions, but the heat-recovery hardware is often exposed to aggressive condensates, high humidity and chemically reactive species that accelerate material degradation.

Shell-and-tube heat exchangers continue to dominate many waste-heat recovery duties because they tolerate high pressure, allow flexible tube layouts and can be maintained using established industrial procedures [7–10]. Their practical reliability, however, is strongly material dependent. In ammonia refrigeration, flue-gas condensation, hydrocarbon processing and acidic or chloride-rich cooling-water services, conventional steels may suffer pitting, crevice corrosion, under-deposit corrosion and stress-corrosion cracking [12–18, 50]. These failure modes reduce heat-transfer area, increase roughness and pressure drop, and may ultimately cause leakage or unplanned shutdown.

For Nigerian and similar developing industrial contexts, the concern is not only chemical aggressiveness but also service variability. High ambient humidity, saline water sources in coastal regions, intermittent maintenance, fluctuating process loads and limited access to specialized replacement parts can intensify corrosion-related downtime [19, 21, 23, 84, 88]. The present study therefore uses Nigeria as an industrial motivation and case context; it does not claim plant-specific validation from a named Nigerian facility. The operating and electrolyte conditions should be interpreted as representative screening conditions for ammonia- and flue-gas-related heat-recovery duties rather than as direct measurements from a particular plant.

Silicon carbide (SiC) has attracted attention for harsh thermal environments because it combines relatively high thermal conductivity, chemical inertness, low thermal expansion and high-temperature stability [25–29]. These properties can reduce thermal resistance and suppress electrochemical degradation compared with metallic alloys. Nevertheless, the literature also shows that SiC heat exchangers face important implementation barriers, including brittleness, thermal-shock sensitivity, machining difficulty, joining/sealing challenges and higher capital cost [27, 29]. Any claim of industrial suitability must therefore be restricted to technical performance under defined conditions and must be separated from full manufacturability, lifecycle-cost and mechanical-integrity qualification.

Recent numerical and modeling studies have expanded the tools available for coupled thermal-hydraulic and electrochemical transport problems relevant to corrosive heat-exchanger service. These include CFD-based shell-and-tube analysis [24, 30, 31], multiphysics heat-transfer and corrosion modeling [32–34], fouling characterization and deposit modeling [35–37], multi-species reactive transport models for localized corrosion prediction [82, 83], electrochemical modeling of CO_2-induced and condensate-driven corrosion in process equipment [85–87], passive film behavior and breakdown on metallic surfaces in chloride-bearing electrolytes [76, 89], localized dissolution kinetics and pitting stability in industrial-grade alloys [90–96], and corrosion-induced wall thinning in heat-exchanger tubes under ammonia and flue-gas service conditions [74, 84]. These studies demonstrate the growing value of coupled electrochemical and transport modeling for material screening and corrosion risk assessment in process industry applications. However, most of them do not directly address the simultaneous thermal-hydraulic and electrochemical screening of SiC versus stainless steel in a shell-and-tube configuration exposed to ammonia thermal service and corrosive flue-gas condensate chemistry.

Accordingly, the contribution of this study is not the invention of new conservation equations or electrochemical laws; the governing equations used are established. The novelty lies in their combined application as a CFD–electrochemical screening framework for comparing SiC and stainless steel in a shell-and-tube waste-heat recovery configuration exposed to ammonia/water thermal service and corrosive flue-gas-condensate chemistry. The study therefore presents the model as a verified, benchmarked and assumption-bounded numerical assessment rather than as an experimentally validated design tool. The objectives are to quantify thermal-hydraulic performance, identify localized electrochemical risk zones, compare material response under identical boundary conditions and define

the limitations that must be addressed in future experimental and techno-economic work.

2 Methodology

2.1 Heat recovery system configuration

A U-tube shell-and-tube heat exchanger representative of industrial waste-heat recovery service was selected as the reference geometry. The U-tube arrangement was retained because it accommodates thermal expansion under large temperature gradients and is widely used where maintenance access and mechanical robustness are important [38–40]. The modeled geometry consists of a cylindrical shell, 16 tubes, baffles and a counter-flow arrangement, as shown in Figure 1. The geometry was used primarily to compare material response under identical flow, thermal and corrosion-boundary conditions rather than to reproduce a proprietary plant exchanger.

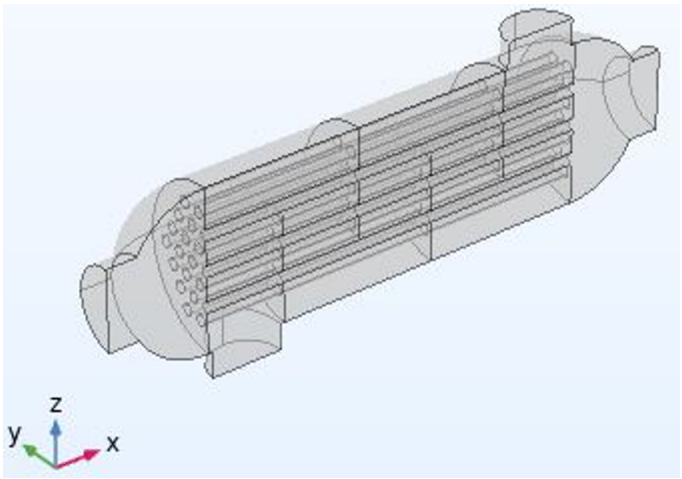

Figure 1. Three-dimensional shell-and-tube heat exchanger model.

Two thermal working fluids were considered in the heat-transfer model: high-pressure ammonia in the tube-side domain and pressurized water in the shell-side domain, as illustrated in Figure 2. The temperatures and pressures were adopted as representative industrial limits from the cited literature [22, 41, 42], while flow-rate values were treated as modeling inputs for comparative screening. This clarification was added because the study is a material-performance comparison, not a plant-data reconciliation exercise.

The key geometric design parameters used in the model (shell and tube dimensions, tube count, baffle configuration, and layout angle) are summarized in Table 1, adopted from established shell-and-tube design references [39, 43].

Table 1. Geometric parameters of the heat exchanger [43].

Parameter	Value
Shell diameter	150 mm
Tube outer diameter	19 mm
Tube inner diameter	16 mm
Number of tubes	16
Tube length	1000 mm
Baffle spacing	200 mm
Baffle cut	25%
Tube layout	Triangular pitch (30°)
Number of baffles	4
Flow Arrangement	Counter-Flow

The geometric configuration described above, together with the thermal and electrolyte boundary conditions introduced in the following subsections, was implemented in COMSOL Multiphysics through the sequential modeling workflow summarized in Figure 3, comprising geometry construction, mesh generation, coupled fluid-thermal-electrochemical physics setup, solution, and verification.

2.2 Materials and thermophysical property definition

Silicon carbide (SiC) was investigated as the candidate heat-exchanger material and benchmarked against stainless steel (SS304), a widely used metallic heat-exchanger material. SiC was selected because it combines high thermal conductivity, chemical inertness, low thermal expansion and reported resistance to chloride- and sulfur-bearing environments [44–46]. Stainless steel was retained as the reference material to enable direct comparison under the same geometry, flow conditions and assumed electrolyte chemistry.

The revised property definition distinguishes between literature property ranges and values actually applied in the base simulation. The base-case SiC values used in the thermal model were density = $3200\,\mathrm{kgm^{-3}}$, specific heat = $670\,\mathrm{Jkg^{-1}K^{-1}}$ and thermal conductivity = $125\,\mathrm{Wm^{-1}K^{-1}}$. The previously reported $170\,\mathrm{Wm^{-1}K^{-1}}$ value is retained only as the upper value in the literature/sensitivity range for dense SiC grades and is not presented as the base-case simulation input [49]. This clarification removes the inconsistency between the earlier Tables 2 and 3 and allows the influence of SiC thermal conductivity to be examined explicitly.

Table 2. Physical properties of the SiC, SS304, and carbon steel.

Material	Density (kg/m^3)	Specific heat (J/kgK)	Thermal conductivity $(Wm^{-1}K^{-1})$	Equivalent uniform roughness $(10^{-3}\,\mathrm{mm})$	Relative roughness (10^{-3})	Thermal diffusivity $(10^{-6}\,\mathrm{m^2s^{-1}})$
Silicon Carbide	3200	670	125 (base case; 90–170 sensitivity range)	0.05	0.025	58.3 (base case)
Stainless Steel	7900	500	15	10	5	3.8
Carbon Steel	7850	780	52	7	4.5	8.5

2.3 Working fluids, operating conditions, and modeling assumptions

Ammonia was selected as the tube-side thermal fluid because of its importance in industrial refrigeration and ammonia-production systems [42]. The thermal model used the ammonia and water streams to resolve heat transfer and pressure drop. The corrosion model was treated separately as an aqueous condensate/electrolyte film at the wetted surface to represent flue-gas-derived corrosive chemistry. The ionic set included chloride (Cl^-), bicarbonate (HCO_3^-), carbonate (CO_3^{2-}), ammonium (NH_4^+), hydroxide (OH^-), bisulfite (HSO_3^-), sulfate (SO_4^{2-}), nitrate (NO_3^-) and hydrogen ions (H^+), consistent with moisture-assisted dissolution of CO_2, SO_x and NO_x species [11, 20, 51–53].

For screening purposes, the flue-gas environment was represented by approximately 70% N_2, 12% CO_2, 8% H_2O vapor, 5% O_2, 0.5% SO_x, 0.3% NO_x and <0.2% particulates by volume [52, 53]. SO_x and NO_x were treated as the principal precursors of acidic condensates. The electrolyte composition is therefore an assumed corrosive boundary condition for comparative material assessment, not a locally sampled Nigerian plant chemistry.

The numerical model was developed under the following bounded assumptions:

- Steady-state thermal-hydraulic operation was assumed, with prescribed inlet temperatures and flow rates.
- The flow equations were solved using a low-Mach-number/incompressible formulation. For high-pressure ammonia, this is a numerical screening simplification; density variation, compressibility and equation-of-state effects were not fully resolved.
- The thermal model was treated as single-phase; boiling, condensation, ammonium-salt deposition and crystallization were outside the scope of the current simulation.

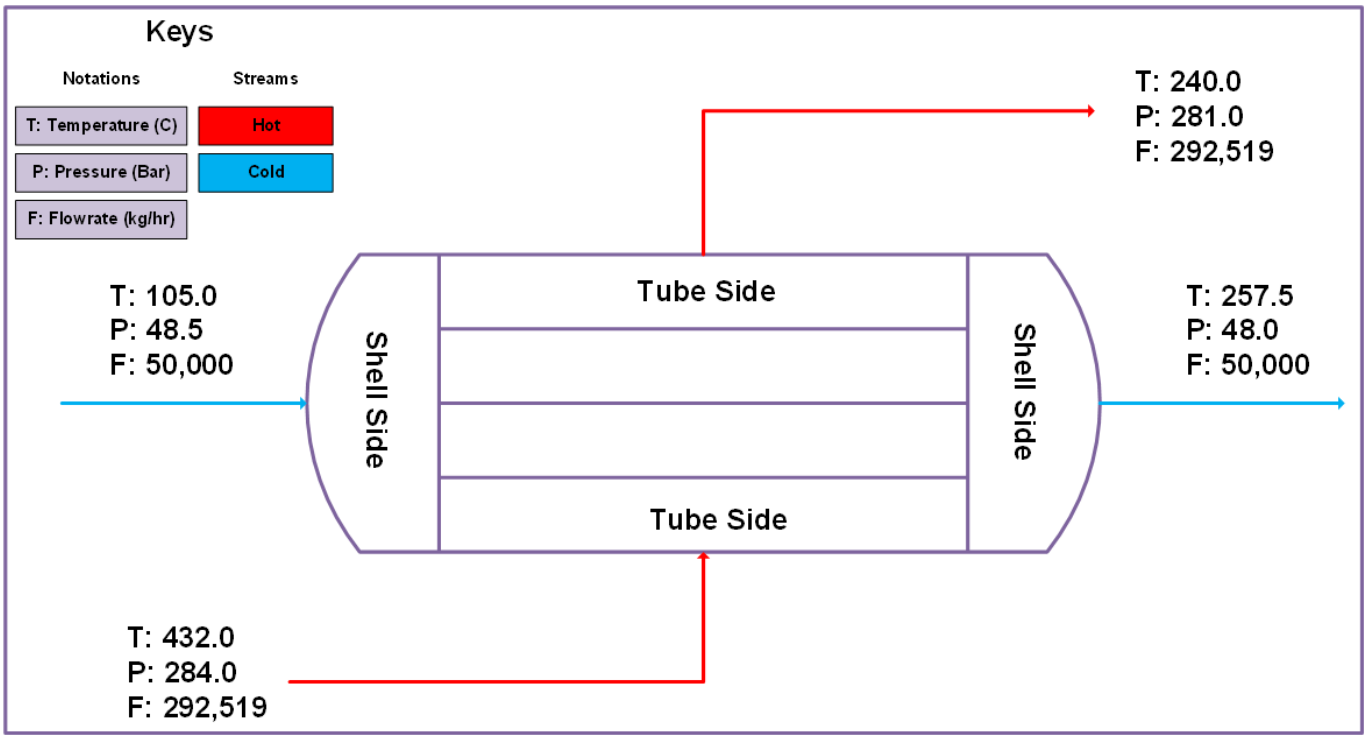

Figure 2. Process flow diagram of waste-heat recovery system.

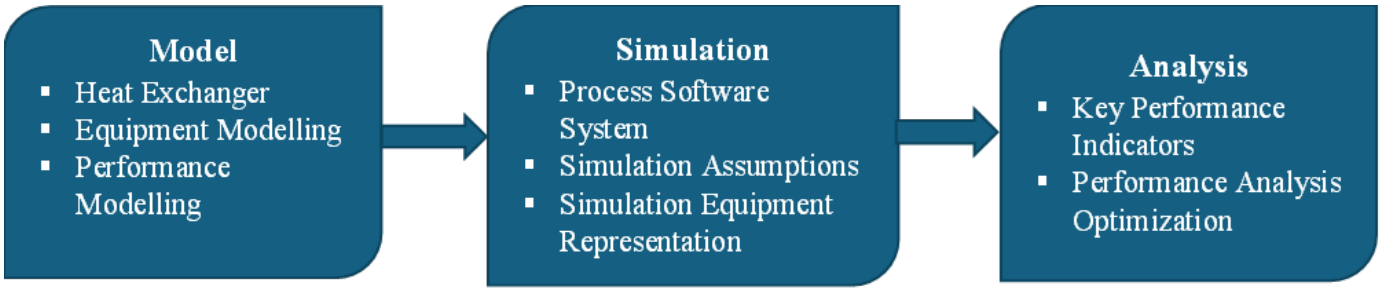

Figure 3. Modeling workflow block diagram.

- Base-case solid properties were treated as constant. The effect of SiC thermal conductivity, roughness and selected electrolyte parameters was examined through sensitivity screening.
- Corrosion was represented through electrochemical boundary coupling and deformed geometry. Explicit solid-state oxidation, passive-film breakdown/repassivation cycles and detailed chemical degradation kinetics were not solved.
- For the corrosion model, the electrolyte was assumed homogeneous and isotropic, and the electrochemical submodel was solved isothermally. The consequence is that predicted corrosion indices should be interpreted as comparative surface-risk indicators, not absolute plant corrosion rates.
- The shell-side corrosion film was treated as laminar and transport-controlled near the interface; turbulent renewal of the electrolyte film was not explicitly resolved.

2.4 Governing equations and physical models

2.4.1 Fluid flow modeling

Fluid flow within the shell and tube domains was modeled using the steady-state conservation of mass and momentum. The continuity and momentum equations used in Eqs. (1) and (2) are standard incompressible Navier–Stokes equations [54]. They are not presented as new mathematical models; their role is to provide the velocity and pressure fields required for thermal-hydraulic comparison and for coupling with near-wall transport in the corrosion assessment.

$$\nabla \cdot \mathbf{u} = 0 \tag{1}$$

$$\rho(\mathbf{u} \cdot \nabla \mathbf{u}) = -\nabla p + \mu \nabla^2 \mathbf{u} \tag{2}$$

where $\mathbf{u}$ is the velocity vector, ρ is the fluid density, p is pressure, and μ is dynamic viscosity.

2.4.2 Heat transfer modeling

Conjugate heat transfer between the fluids and solid exchanger walls was resolved by coupling the energy equation in the fluid domains with conduction in the solid regions [55]. Eqs. (3) and (4) are likewise standard energy and conduction equations. The model contribution is the coupling of these equations with species transport and electrochemical boundary reactions so that thermal performance and corrosion susceptibility are assessed within the same exchanger geometry.

$$\rho c_p(\mathbf{u} \cdot \nabla T) = \nabla \cdot (k \nabla T) \tag{3}$$

$$\rho c_p \frac{\partial T}{\partial t} = \nabla \cdot (k \nabla T) \tag{4}$$

Table 3. Summary of material properties applied in the simulation [48, 56, 57].

Material	Density ($\mathrm{kg/m^3}$)	Specific Heat ($\mathrm{J/kg\,K}$)	Thermal Conductivity ($\mathrm{W/m\,K}$)	Young's Modulus (Pa)
Ammonia (tube)	682	4700	0.52	—
Water (shell)	997	4180	0.6	—
Stainless Steel	7900	500	15	2.0×10^{11}
Silicon Carbide	3200	670	125	4.0×10^{11}

Material properties applied in simulation (ammonia, water, SS, SiC) are listed in Table 3.

2.5 Electrochemical corrosion modeling

Electrochemical corrosion at the material–electrolyte interface was modeled by treating the shell-side condensate film as an ionic electrolyte [58]. Corrosion behavior was simulated in COMSOL Multiphysics 6.1 using a time-dependent framework coupling Secondary Current Distribution (SCD), Transport of Dilute Species (TDS) and Deformed Geometry (DG). A tertiary current-distribution/Nernst–Planck formulation was also used to resolve ionic diffusion, migration and convection. These equations are established electrochemical transport relations; the present work applies them to compare SiC and stainless steel surfaces under the same assumed corrosive condensate. The corresponding material sectional configuration used for the corrosion submodel—comprising the candidate tube material (SiC or stainless steel), the supporting shell structure, and the adjacent electrolyte domain—is shown in Figure 4.

Figure 4. Material sectional view for corrosion model.

The electrochemical corrosion model relates surface degradation rate to local concentration of corrosive agents through Eq. (5). The general species mass-balance equation is given by Eqs. (6) and (7), where Eq. (6) is the conservation statement and Eq. (7) defines the molar flux N_i for the dilute (non-migrative) case.

$$R_i = k_{\text{corr}}(T) C_i \tag{5}$$

$$\frac{\partial c_i}{\partial t} + \nabla \cdot N_i = R_i \tag{6}$$

$$N_i = -D_i \nabla c_i + c_i \mathbf{u} \tag{7}$$

where R_i is corrosion reaction rate, T temperature, and C_i local concentration, D_i is diffusion coefficient and $\mathbf{u}$ convective velocity.

The electrolyte ionic set (minimal useful set) included H^+, OH^-, HCO_3^-, CO_3^{2-}, HSO_3^-, SO_3^{2-}, SO_4^{2-}, NO_2^-, NO_3^-, Cl^-, NH_4^+, consistent with flue-gas dissolution and aqueous acid/base pathways [58, 59].

Furthermore, the electrochemical potential in the electrolyte satisfies the expression in Eq. (8), and the charge-transfer kinetics at the interface were modeled using the Butler–Volmer relation in Eq. (9).

$$\nabla \cdot (\kappa \nabla \phi) = 0 \tag{8}$$

$$i = i_0 \left[\exp\left(\frac{\alpha_a F \eta}{RT} \right) - \exp\left(-\frac{\alpha_c F \eta}{RT} \right) \right] \tag{9}$$

where κ is electrolyte conductivity and ϕ electric potential, i_0 is exchange current density, α_a, α_c transfer coefficients, F Faraday constant, R gas constant, T temperature, and η overpotential.

Wall recession was linked to corrosion current density through Faraday's law expressed in Eq. (10). In addition, a tertiary current distribution (Nernst-Planck) model was employed to account for ion diffusion, migration, and convection. The ionic flux for each species i is defined using Eq. (11) [60, 61].

$$\nu_n = -\frac{M}{nF\rho} i_{\text{corr}} \tag{10}$$

where ν_n is normal mesh velocity, M molar mass of iron, n electrons transferred, ρ metal density, and i_{corr} obtained from SCD.

$$N_i = -D_i \nabla c_i - z_i u_i F c_i \nabla \phi + c_i \mathbf{u} \tag{11}$$

2.6 Boundary and initial conditions

At the electrolyte inlet, prescribed velocity and bulk concentrations were defined for each ionic species. The outlet was specified using a convective-flux condition with zero diffusive flux, which imposes $\mathbf{n} \cdot (-D_i \nabla c_i) = 0$ while allowing species to leave the domain by advection. This condition is appropriate where the outlet is sufficiently far from the reacting surface and avoids artificial concentration back-diffusion into the computational domain. The inner wall surface was defined as the electrochemical boundary, where current distribution and deformed-geometry

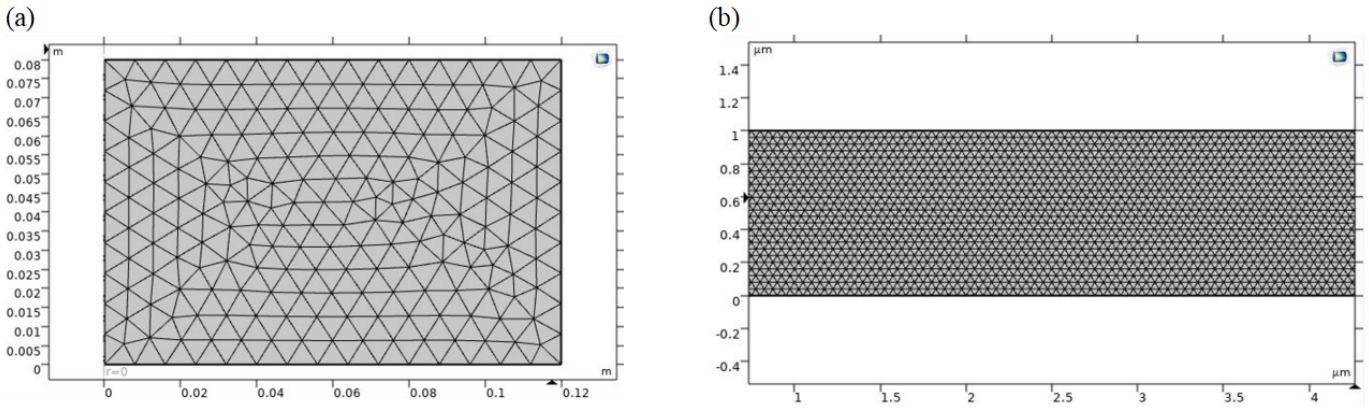

Figure 5. Mesh model for corrosion modelling using (a) electrochemical reactions at the metal–electrolyte interface, (b) tertiary current distribution (Nernst-Planck) approach.

wall recession were coupled. Initial conditions assumed uniform bulk concentration and zero initial overpotential.

The inward fluxes and equivalent current densities used in the study are provided in Table 4 (computed using $k_c = 1 \times 10^{-4}\,\mathrm{m\,s^{-1}}$ and $F = 96\,485\,\mathrm{C\,mol^{-1}}$).

Table 4. Inward fluxes N_i and equivalent current densities j_i.

Species	Charge (z_i)	c_{bulk} ($\mathrm{mol\,m^{-3}}$)	($N_i = k_c c$) ($\mathrm{mol\,m^{-2}\,s^{-1}}$)	$j_i = z_i F N_i$ ($\mathrm{A\,m^{-2}}$)
H^+	+1	1.0×10^{-7}	1.0×10^{-11}	9.65×10^{-7}
OH^-	-1	1.0×10^{-7}	1.0×10^{-11}	-9.65×10^{-7}
HCO_3^-	-1	3.0	3.0×10^{-4}	-28.95
CO_3^{2-}	-2	1.0×10^{-4}	1.0×10^{-8}	-1.93×10^{-3}
HSO_3^-	-1	1.0×10^{-1}	1.0×10^{-5}	-0.965
SO_4^{2-}	-2	1.0×10^{-1}	1.0×10^{-5}	-1.93
NO_3^-	-1	1.0×10^{-2}	1.0×10^{-6}	-0.0965
Cl^-	-1	1.0×10^{-3}	1.0×10^{-7}	-0.00965
NH_4^+	+1	1.0×10^{-4}	1.0×10^{-8}	+0.000965

$$D_{\mathrm{Cl^-}} = 2.0 \times 10^{-9} \quad D_{\mathrm{O_2}} = 2.0 \times 10^{-9}$$
$$D_{\mathrm{CO_2}} = 1.9 \times 10^{-9} \quad D_{\mathrm{H_2}} = 4.5 \times 10^{-9} \quad n = 2$$

Electrolyte conductivity was set to $0.5\,\mathrm{S\,m^{-1}}$ in the base case and varied in the sensitivity screening. Diffusion coefficients were assigned from dilute aqueous electrolyte values reported in the literature for the included ionic species. Carbon steel properties used for corrosion-wall recession included density $7850\,\mathrm{kg\,m^{-3}}$, molar mass $55.85\,\mathrm{g\,mol^{-1}}$ and electron-transfer number for Fe dissolution [47]. Because the electrochemical submodel was not calibrated against in-house polarization measurements, the predicted current-density and wall-recession values are used as relative material indicators.

2.7 Meshing and numerical solution

A physics-controlled mesh was applied with refinement at the metal-electrolyte interface to resolve steep concentration and potential gradients as presented in Figure 5. Mesh independence study was performed to confirm that further refinement did not significantly change predicted corrosion metrics. For the heat transfer and flow model, a segregated solver strategy was employed by solving flow fields first, then temperature fields, followed by coupling with wall conduction [62]. Iterative solvers (GMRES with ILU preconditioning) were used to reduce memory requirements. For the corrosion model, a time-dependent solver was used over 0–100 s, with the Backward Differentiation Formula (BDF) method and a maximum time step of 10 s. Automatic re-meshing was enabled to accommodate progressive material loss during deformation.

To ensure accurate coupling between the SiC tube domain, carbon steel shell domain, and fluid domains, the geometry was created as separate domains and joined using Boolean Assembly operations (not Union). Identity pairs were defined at shared interfaces to enforce continuity of temperature/heat flux and electrochemical potential/ionic flux across nonconformal meshes.

Thermal continuity at the solid-fluid interface was enforced using Eq. (13), while the electrochemical continuity for corrosion modeling was imposed using Eq. (14).

$$T_{\mathrm{tube}} = T_{\mathrm{shell}} \qquad q_{\mathrm{tube}} = q_{\mathrm{shell}} \tag{12}$$

$$\phi_{\mathrm{tube}} = \phi_{\mathrm{shell}} \qquad \mathbf{n} \cdot \mathbf{J}_{\mathrm{tube}} = \mathbf{n} \cdot \mathbf{J}_{\mathrm{shell}} \tag{13}$$

Pair compatibility checks were used to verify smooth data transfer across interfaces. Proper merging was confirmed by continuous gradients in temperature and current density profiles across the interfaces, consistent with COMSOL workflow guidance [63].

2.8 Convergence analysis

Convergence analysis was conducted to ensure that the numerical solution was not dominated by mesh size, time-step selection or solver tolerance. Four mesh levels were tested by monitoring total heat-transfer rate (Q), outlet wall temperature and current density. A relative deviation below 2% between successive mesh levels was used as the mesh-independence criterion.

$$E(\%) = \frac{|R_n - R_{n-1}|}{R_n} \times 100 \tag{14}$$

where R_n and R_{n-1} are the results from successive mesh refinements. A deviation below 2% was considered indicative of mesh-independent results.

Solver convergence was also assessed by monitoring the residuals of governing equations during iterations. The convergence criteria used in this study for each physics interface is presented in Table 5.

Table 5. Convergence criteria.

Physics	Residual Tolerance	Type of Study
Heat Transfer	10^{-6}	Stationary
Fluid Flow	10^{-5}	Stationary
Electrochemistry (SCD)	10^{-4}	Time-dependent

Residuals were monitored until monotonic decay was obtained. Where oscillation occurred, time-step control and damping were applied. Numerical convergence is reported as solver verification only; it does not constitute experimental validation.

2.9 Model verification, literature benchmarking, and uncertainty treatment

Because new experimental testing was not available for the study, the model is described as verified and benchmarked rather than fully validated. Verification consisted of mesh-independence checks, residual convergence monitoring, heat-duty consistency checks and comparison of qualitative trends against published CFD/experimental heat-exchanger and electrochemical corrosion studies. The available benchmark literature reports the same expected tendencies: stronger local heat flux near inlet/baffle regions, pressure-loss concentration around flow-redirection zones, localized current-density amplification near reactive boundaries, and chloride-driven destabilization of metallic passive films [17, 18, 43, 68, 75–81] (see Table 6).

3 Results and discussion

3.1 Electrochemical corrosion behavior at the steel-electrolyte interface

Figure 6 presents the spatial distribution of electrode potential coupled with electrolyte current-density streamlines at the steel–electrolyte interface. The potential varies between approximately -1.44 and -1.58 V, producing a lateral potential difference of about 0.14 V across the steel surface. This potential difference is sufficient to drive spatially non-uniform anodic and cathodic regions in a conductive electrolyte [64, 65]. The result is therefore interpreted as evidence of localized electrochemical driving force, not as direct proof of measured plant corrosion rate.

This interpretation is reinforced by the directional current components reported in Figure 7, where the x-component of electrolyte current density remains predominantly negative (-1 to -11 A·m^{-2}), indicating sustained ionic migration toward the steel surface, while the y-component shows a symmetric distribution

Table 6. Model verification and literature benchmarking.

Benchmark item	Expected trend from literature	Present model response	Interpretation
Temperature field	Largest thermal driving force near inlet and baffle-influenced regions	Steepest gradients occurred near inlet/outlet and baffle zones	Trend agreement; supports qualitative heat-transfer behavior
Pressure field	Flow redirection and baffle windows increase local pressure loss	Pressure contours showed localized losses near tube ends and baffles	Trend agreement; not a plant pressure-drop validation
Electrochemical field	Current density localizes at reactive metal/electrolyte interfaces	Peak current density concentrated near the wall boundary	Trend agreement with corrosion theory
Species transport	Bulk concentration may remain nearly uniform while near-wall gradients control reaction rate	Flat bulk concentration curves with localized interfacial current-density gradients	Explains concentration-plot appearance and localized corrosion risk

Table 7. Screening-level uncertainty analysis.

Parameter varied	Base value	Screening range	Primary effect on result	Study interpretation
SiC thermal conductivity	125 $\mathrm{W\,m^{-1}\,K^{-1}}$	90–170 $\mathrm{W\,m^{-1}\,K^{-1}}$	Changes wall conduction resistance and predicted U/h^{-1}	The 47.6% heat-transfer improvement is a base-case prediction, not a universal material constant
Equivalent roughness	0.05×10^{-3} mm	±50%	Affects pressure drop and near-wall turbulence	Hydraulic benefit should be checked for manufactured tube finish
Electrolyte conductivity	0.5 $\mathrm{S\,m^{-1}}$	0.25–1.0 $\mathrm{S\,m^{-1}}$	Scales ionic migration and current density	Corrosion-current magnitudes are chemistry dependent
Chloride concentration	1.0×10^{-3} $\mathrm{mol\,m^{-3}}$	0.5–5.0 $\times 10^{-3}$ $\mathrm{mol\,m^{-3}}$	Controls passive-film destabilization and local corrosion tendency	Corrosion reduction is reported as a comparative model indicator
Boundary temperatures	Base operating case	±5%	Changes local heat flux and electrolyte reactivity if thermally coupled	Thermo-electrochemical coupling remains future work

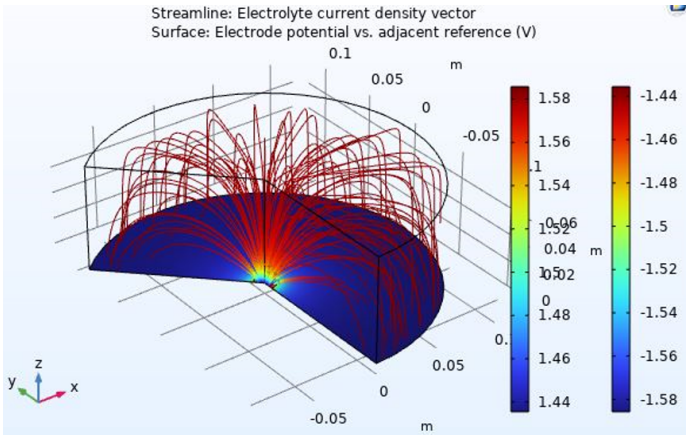

Figure 6. Electrolyte current density and electrode potential distribution.

about the mid-plane. Together, these results confirm that electrochemical activity is preferentially focused at the metal-electrolyte interface rather than being evenly distributed throughout the electrolyte domain.

A screening-level uncertainty analysis was added to quantify the robustness of the material comparison as depicted in Table 7. The analysis used the base-case outputs and varied the most influential uncertain inputs: SiC thermal conductivity (90–170 $\mathrm{W\,m^{-1}\,K^{-1}}$), wall roughness (±50%), electrolyte conductivity (0.25–1.0 $\mathrm{S\,m^{-1}}$) and chloride concentration (0.5–5.0 $\mathrm{mmol\,m^{-3}}$). Because the exact plant chemistry and experimental polarization curves were not available, the ranges are presented as uncertainty bounds for preliminary screening rather than statistical confidence intervals.

3.2 Localized current density amplification and corrosion severity

The absolute electrolyte current-density field shown in Figure 8(a) indicates peak values above 200 A $\mathrm{m^{-2}}$ at limited regions of the steel boundary, while the bulk electrolyte remains much lower. Faraday's law links local corrosion penetration to current density; therefore, small surface zones with high current density can dominate wall-loss risk even when the average current is moderate [66–68]. This interpretation is consistent with industrial heat-exchanger failures that occur by pitting or localized perforation rather than by uniform thinning.

This behavior is characteristic of localized corrosion, where the electrochemical driving force is confined to narrow interfacial regions rather than uniformly distributed across the surface [65, 71]. For the SiC case, the predicted current-density and potential fields are more spatially restrained than for stainless steel under the same assumed electrolyte chemistry. This finding is consistent with the known chemical inertness and electrical resistance of SiC; however, the conclusion is framed as a modeled comparative tendency because experimental polarization tests were not performed in this study.

3.3 Electrolyte potential gradients and confinement of corrosion activity

Figure 9 illustrates the electrolyte potential field overlaid with current density streamlines. The potential field varies between approximately 1.44 V and 1.58 V. Regions near the tube wall exhibit sharper gradients, which are associated with intense anodic or cathodic reaction sites. The current density streamlines converge towards these boundaries,

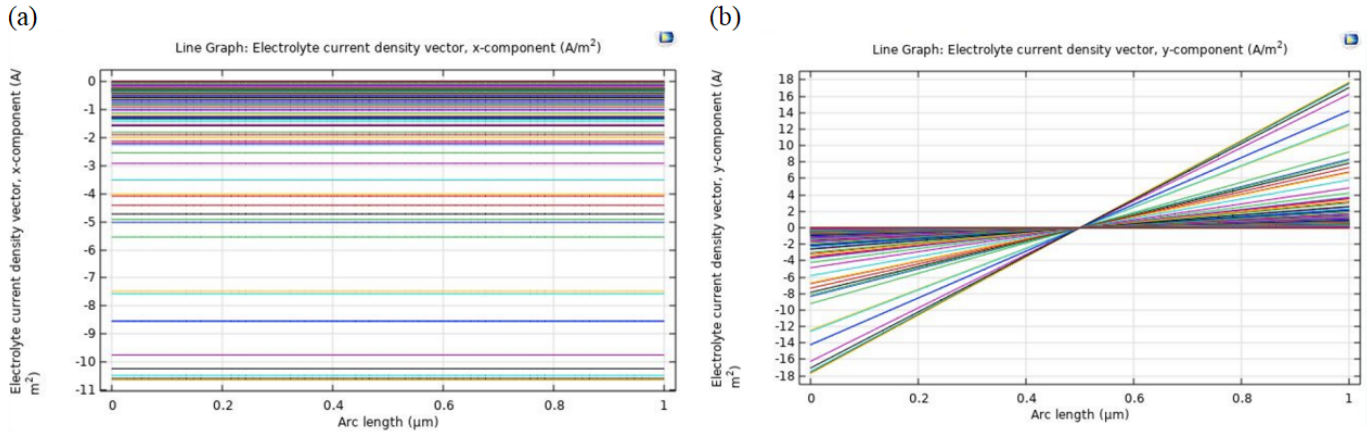

Figure 7. Electrolyte current density vector, (a) x-component, (b) y-component.

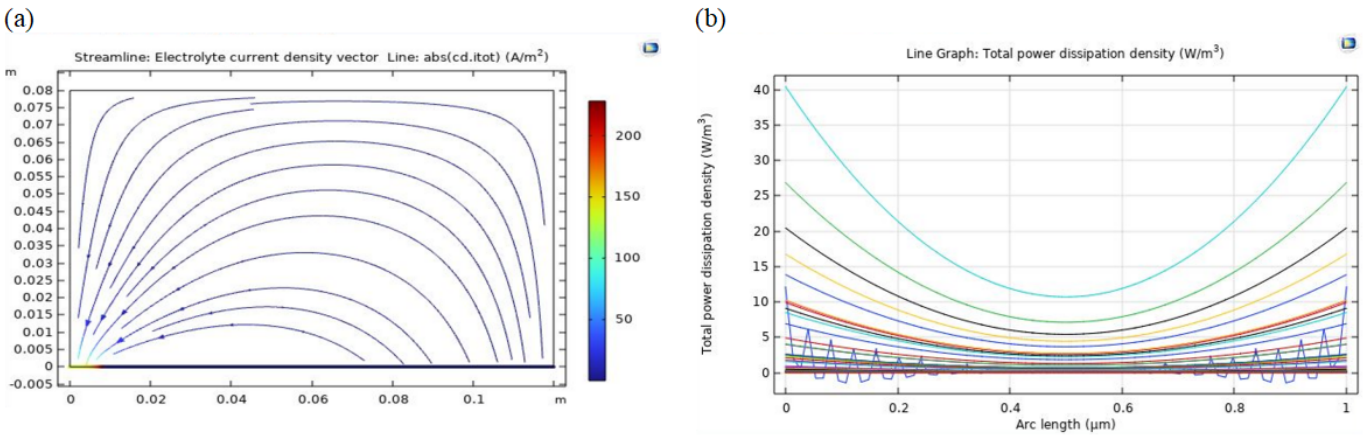

Figure 8. (a) Electrolyte current density streamlines, (b) Total power dissipation density.

confirming localized electrochemical activity at the wall electrolyte interface. This confinement indicates that corrosion kinetics are governed by interfacial transport limitations rather than depletion of reactive species in the bulk [68, 69]. This is consistent with the nearly uniform bulk concentration profiles shown in Figure 9, where species concentrations remain relatively constant away from the boundary layer. The combined evidence confirms that localized corrosion cannot be inferred from bulk water chemistry alone, but is instead controlled by near-wall electrochemical and transport phenomena.

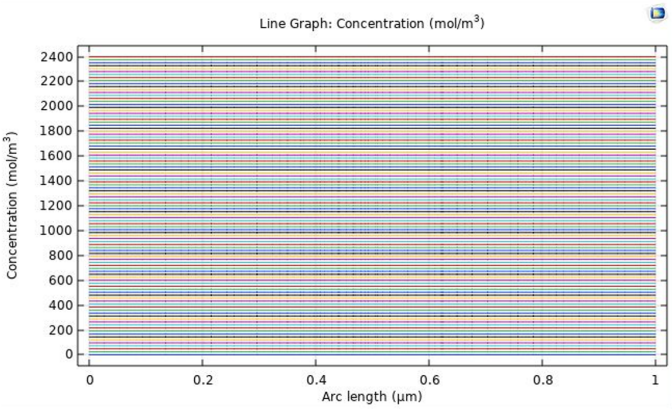

Figure 9. Bulk species concentration diagnostic.

Figure 9 further shows the concentration diagnostic used to examine bulk species distribution. The concentration lines appear nearly flat because the plotted scale is dominated by the imposed homogeneous bulk electrolyte, and because the steepest concentration changes occur within a thin near-wall boundary layer that is not readily visible in the full-domain line plot. This does not mean that the corrosion model is insensitive to chemistry; rather, it indicates that the dominant corrosion response in the present case is governed by interfacial potential/current-density gradients and near-wall transport rather than by depletion of the entire bulk electrolyte [68, 69].

Figure 10 (a) presents the surface distribution of electrolyte potential within the shell-side domain, overlaid with current density streamlines to illustrate charge transport pathways. The potential varies

between approximately 1.44 V and 1.58 V, with the steepest gradients occurring at the tube wall electrolyte interface, particularly in the lower-left region of the domain. These steep gradients indicate zones where electrochemical reactions are most active, encompassing both anodic metal dissolution and cathodic reduction reactions such as oxygen or hydrogen reduction. The dense clustering of current streamlines near the wall confirms that electrochemical activity is strongly concentrated at the material boundary, while the gradual divergence of streamlines into the bulk electrolyte reflects the dissipation of electrochemical influence away from the interface [68–70].

This behavior is characteristic of localized corrosion phenomena, where the electrochemical driving force is confined to narrow boundary-layer regions rather than being uniformly distributed across the surface [65, 71]. Importantly, when silicon carbide (SiC) is employed as the tube wall material, the potential field remains relatively uniform across most of the electrolyte domain, with only limited regions exhibiting sharp potential drops. This observation reflects the chemical inertness and electrochemical stability of SiC, which suppresses extensive anodic dissolution and restricts corrosion activity to small, isolated regions. In contrast, simulations performed with metallic tube materials such as stainless steel show broader potential gradients and more diffuse current paths, indicating a higher susceptibility to generalized corrosion and widespread surface degradation [72, 73]. These results have direct implications for heat exchanger durability. Localized electrochemical hot spots on steel surfaces can progressively develop into pitting corrosion, leading to wall thinning, loss of mechanical integrity, and a gradual decline in heat transfer performance over time [71, 74]. By maintaining a more stable and uniform potential distribution, SiC minimizes these risks, thereby enhancing both the structural longevity and thermal reliability of heat exchangers operating in corrosive environments.

Additionally, Figures 10 (b) and (c) present results obtained using the tertiary current distribution (Nernst-Planck) formulation, which explicitly accounts for ionic migration, diffusion, and convection within the electrolyte. The electrolyte potential field in Figure 10 (b) exhibits pronounced gradients near the tube wall, where the highest anodic potential values are concentrated. These regions correspond to sites of intense metal dissolution, confirming that the wall remains the dominant locus of corrosion activity. The smooth decay of potential toward the bulk fluid highlights the role of electrolyte transport in redistributing charge away from the interface, demonstrating that while corrosion reactions are surface-dominated, they are strongly modulated by ion transport within the adjacent electrolyte layer [69, 73]. The electrolyte potential distribution in Figure 10 (c) reveals a nearly uniform gradient. The parallel potential lines show that the applied or induced potential is distributed smoothly across the electrolyte domain, while the strongest reaction-driving gradients remain near the wall. Comparable behavior has been reported in electrochemical transport simulations where migration and diffusion redistribute charge away from the interface [75, 76].

The electrolyte current density vectors shown in Figure 10 (d) provide complementary insight into this process. Maximum current densities exceeding 3 $A \cdot m^{-2}$ are observed in localized regions adjacent to the corroding surface, directly correlating with elevated local corrosion rates. Away from the wall, current density decreases rapidly, indicating that charge transfer reactions are confined to the interface and sustained by migration and diffusion of ions from the bulk electrolyte. The largely symmetric distribution of current density vectors across the fluid domain suggests that ionic migration and diffusion act as the primary mechanisms balancing charge transport, rather than bulk convection. As a result, corrosion rate predictions derived from the local current density field offer a realistic and physically consistent measure of localized material degradation, in agreement with established electrochemical corrosion theory [77].

3.4 Role of silicon carbide in restricting corrosion spread

The current density distribution in Figure 11 shows that high-current regions remain sharply confined to the steel–electrolyte boundary and do not propagate along the silicon carbide tube surface. This behavior reflects the chemical inertness and high electrical resistivity of SiC, which prevents anodic dissolution and suppresses galvanic coupling with steel [72, 78].

The electrochemical stability of the SiC–steel configuration is further supported by the smooth convergence behavior observed in Figure 12 (a), where the electrochemical reaction model stabilizes without oscillatory divergence. Such numerical stability is typically associated with physically stable electrochemical systems and contrasts with metallic systems that experience repeated passive-film

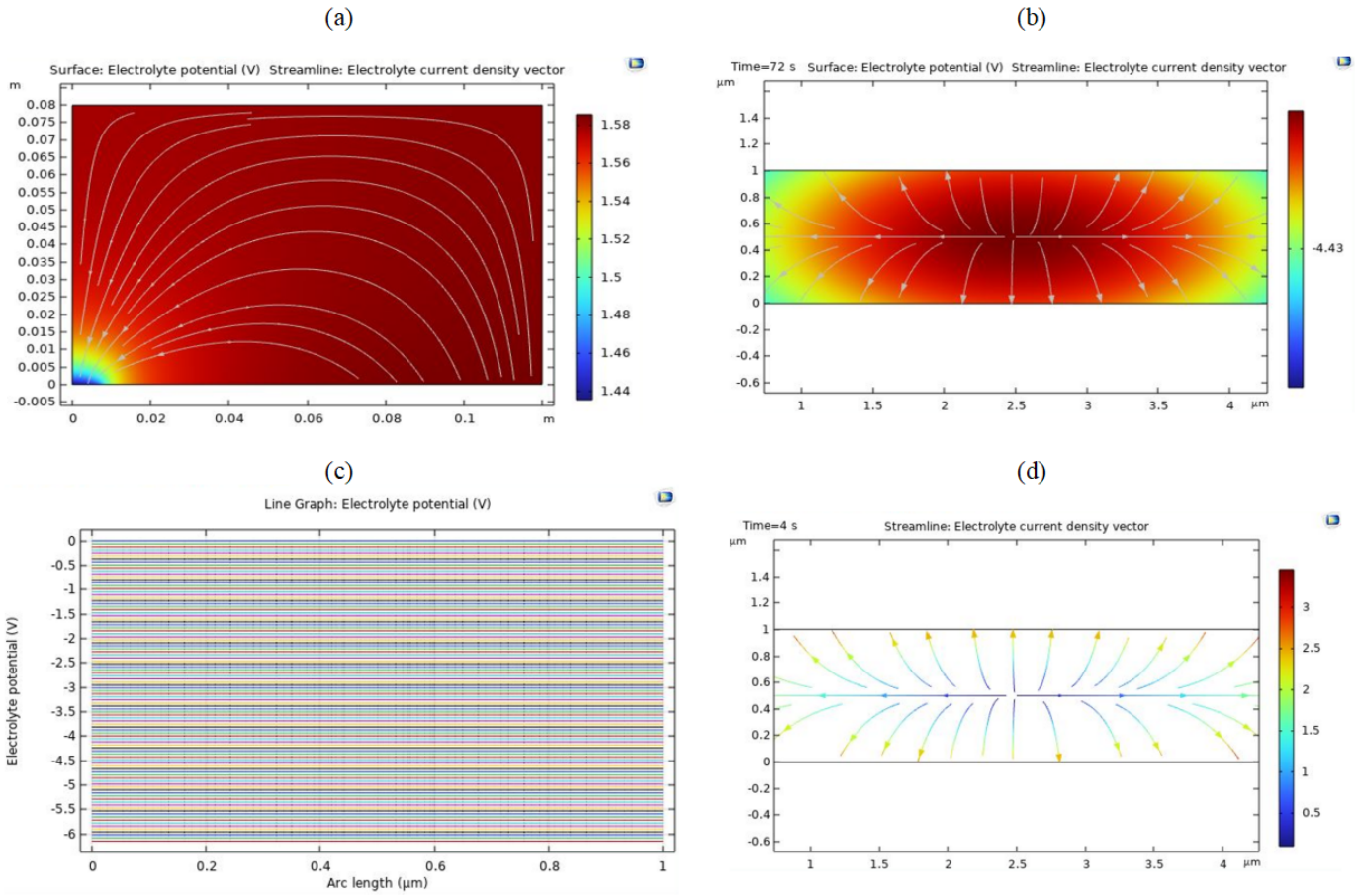

Figure 10. (a) Surface distribution of electrolyte potential, (b) Electrolyte potential field from tertiary current distribution model (Nernst–Planck), (c) Electrolyte potential contour lines (V), (d) Electrolyte current density vector.

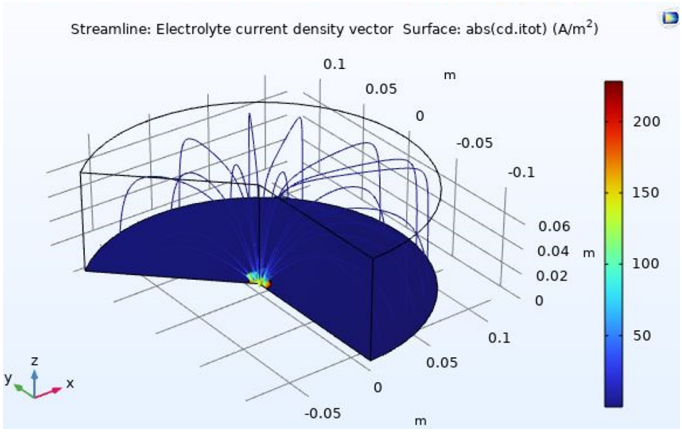

Figure 11. Absolute current density distribution and vector field in electrolyte.

breakdown [67, 72].

Figure 12 (b) corresponds to the tertiary current distribution model based on the Nernst–Planck equations, which account for ion transport by migration, diffusion, and convection in the electrolyte domain. Similar to the electrochemical model, the solver begins with small time steps (high reciprocal values), indicating a dynamic adjustment to the strong concentration and potential gradients present at the early stage of simulation.

As time progresses, a stepwise reduction in the reciprocal of step size can be observed between time steps 5 and 25, which represents the solver's adaptive time stepping in response to the non-linear coupling between ionic concentration and electric potential distribution. After approximately time step 27, the solver reaches a plateau, indicating convergence to a steady ionic flux and potential field throughout the computational domain.

This convergence pattern is typical of tertiary current-distribution simulations after initial charge redistribution. The plateau indicates numerical stabilization of the ionic-flux and potential fields. It should be noted that solver stability demonstrates numerical convergence, not physical validation; the corrosion predictions still require comparison with polarization or immersion tests for design-level use.

3.5 Species-resolved corrosion mechanisms and ionic synergy

The tertiary current distribution results provide deeper insight into the chemical drivers of corrosion. The hydrogen ion distribution in Figure 13 (a) shows maximum flux values approaching $796\,\mathrm{mol\,m^{-3}\,s^{-1}}$ near the steel surface, indicating localized acidification at anodic sites. Simultaneously, Figure 13 (b) shows hydroxide ion accumulation (up to 2.41×10^{-5} $\mathrm{mol\,m^{-3}}$) near cathodic regions, reflecting oxygen reduction reactions.

These pH micro-gradients are sustained by bicarbonate transport shown in Figure 13 (c), where inward HCO_3^- flux supports carbonic-acid-driven corrosion [68]. The effect is intensified by bisulfite transport in Figure 13 (d), where HSO_3^- depletion near the interface indicates active participation in redox reactions that generate additional acidity [68, 79]. The aggressive nature of the environment is dominated by chloride behavior in Figure 13 (e), which shows chloride accumulation near the steel surface ($0.24\,\mathrm{mol\,m^{-3}}$). Despite its low bulk concentration, chloride's interfacial enrichment destabilizes protective films and initiates localized attack [79].

Importantly, the evolution of ammonium ions shown in Figure 13 (f) (reaching $-1.82\,\mathrm{mol\,m^{-3}}$ at later times) explains why these localized reactions are sustained. NH_4^+ increases electrolyte conductivity, facilitating higher ionic current flow and accelerating corrosion once initiated, even though the ion itself is not chemically aggressive [68]. Carbonate ions, shown in Figure 13 (g), remain at low concentrations ($0.02\,\mathrm{mol\,m^{-3}}$) and exhibit primarily diffusive transport, indicating limited passivation or buffering capability under the studied conditions.

3.6 Heat transfer and fluid flow analysis

The temperature contour plots shown in Figure 14(a) illustrate the thermal behavior of the shell-and-tube heat exchanger under the specified screening conditions. The tube-side stream cools along the exchanger length while the shell-side stream absorbs heat. The strongest thermal gradients occur near the inlet/outlet and baffle-influenced regions where the local temperature difference is largest. This is consistent with conventional shell-and-tube exchanger theory and published CFD studies showing high local heat flux near the inlet and redirection zones [68, 80].

The pressure distribution in Figure 14(b) shows localized losses near tube inlets, outlets and baffle regions. These losses arise from viscous friction and repeated flow redirection. The absolute pressure-drop values should be interpreted comparatively because the model uses idealized surfaces and prescribed operating conditions. Nevertheless, the relative reduction predicted for SiC is useful for material screening because roughness, wall heat transfer and near-wall velocity structure influence both hydraulic resistance and long-term fouling/corrosion risk.

Furthermore, for a compact engineering comparison, two additional indices were calculated from the base-case outputs. The percentage heat-transfer improvement was computed as $[(620 - 420)/420] \times 100 = 47.6\%$, the pressure-drop reduction as $[(2.63 - 1.92)/2.63] \times 100 = 27.0\%$, and the thermal–hydraulic performance factor as $(h_{\mathrm{SiC}}/h_{\mathrm{SS}})/(\Delta P_{\mathrm{SiC}}/\Delta P_{\mathrm{SS}})^{1/3} = 1.64$. These indices are now reported in the Table 8 to reduce reliance on contour-plot interpretation alone. However, summary of the comparative performance

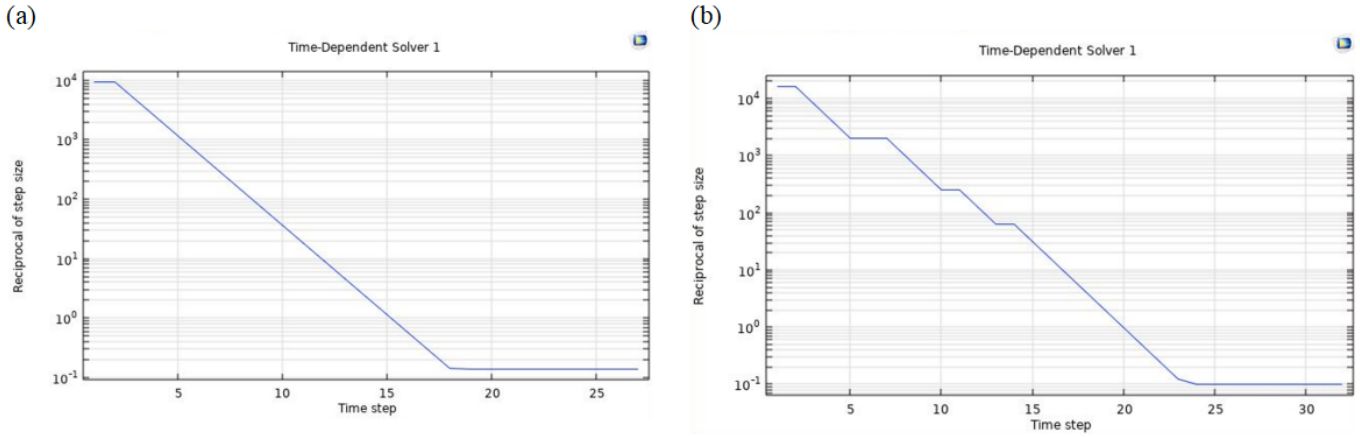

Figure 12. Convergence plot for corrosion modelling using (a) electrochemical reactions at the metal–electrolyte interface (b) tertiary current distribution (Nernst–Planck) approach.

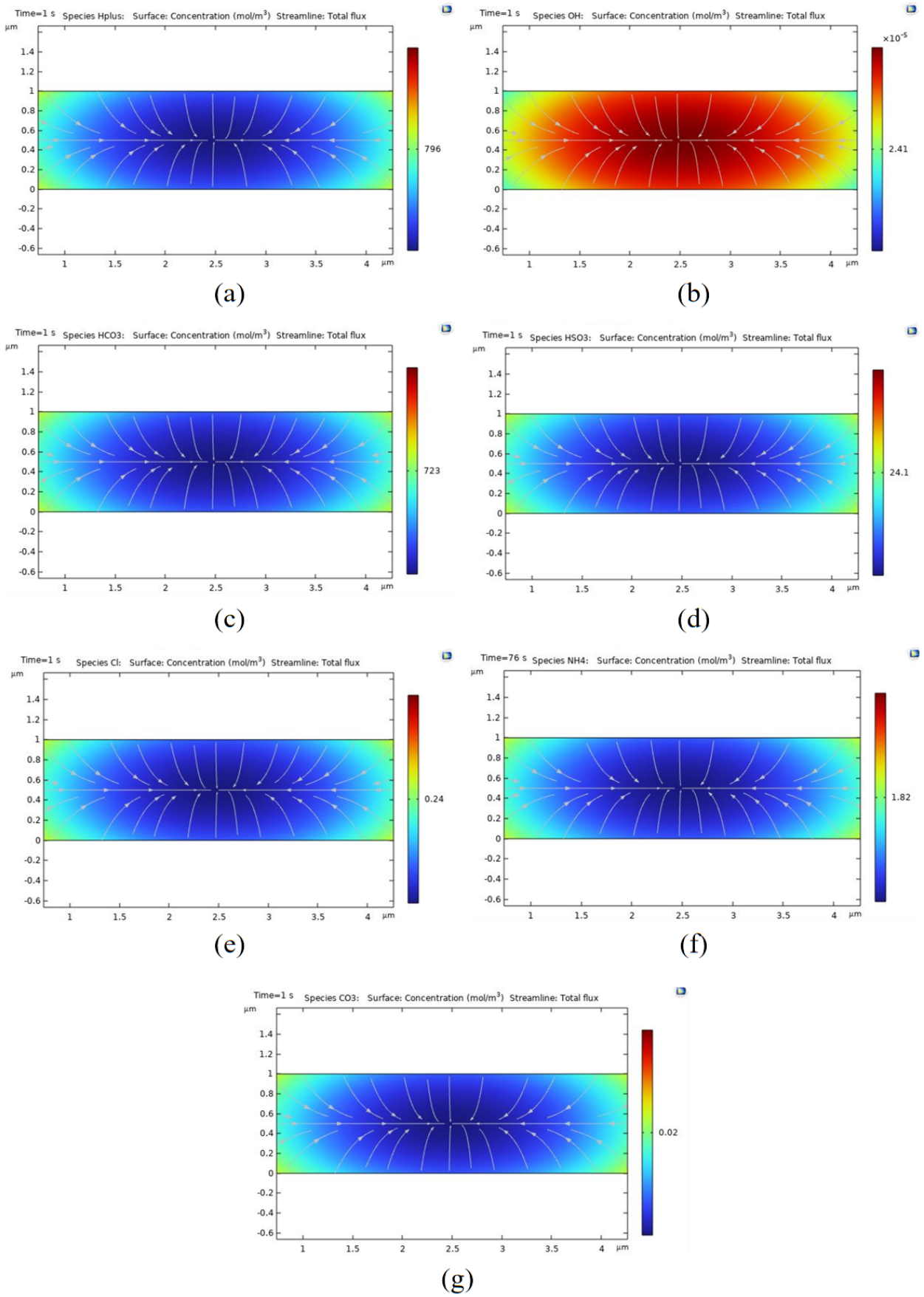

Figure 13. Surface concentration distribution of (a) H^+, (b) OH^-, (c) HCO_3^-, (d) HSO_3^-, (e) Cl^-, (f) NH_4^+ and (g) CO_3^{2-}.

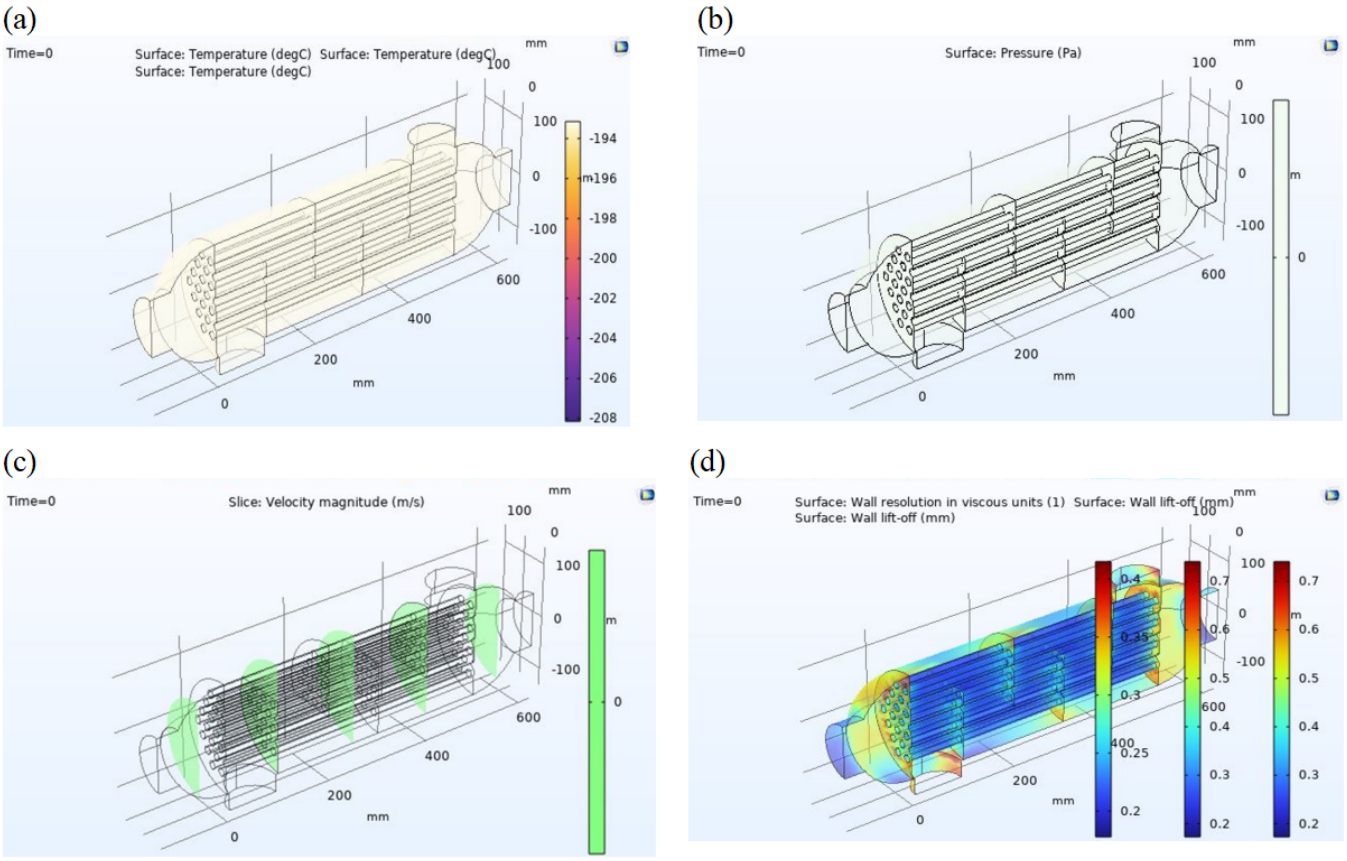

Figure 14. (a) Surface temperature plot, (b) surface pressure plot, (c) surface velocity plot and (d) wall effects/flow distribution of the heat exchanger.

metrics studied for stainless steel and SiC are presented in Table 8.

3.7 Practical implementation and industrial limitations

Although the numerical results favor SiC, industrial deployment requires additional mechanical and economic qualification. SiC is brittle compared with metallic alloys and can be sensitive to impact, tensile stress concentration and thermal shock. Tube-to-tube-sheet joining, sealing, inspection, repair, manufacturing tolerance and replacement logistics may also increase capital cost. In large shell-and-tube units, hybrid designs may be more realistic than all-SiC construction, for example SiC tubes or liners combined with metallic support structures, compliant seals and thermal-expansion allowances.

For process industries, the strongest near-term relevance of this work is material-screening guidance for services where metallic exchangers repeatedly suffer corrosion or fouling. The results do not yet justify immediate plant-wide replacement of stainless-steel exchangers. A practical adoption pathway should include coupon-scale electrochemical testing in locally sampled condensates, thermal-shock and mechanical-integrity testing, pilot-scale exchanger trials, lifecycle-cost analysis and maintenance-supply-chain assessment.

4 Conclusion

This study developed a coupled CFD-electrochemical numerical framework for comparing silicon carbide and stainless steel in a shell-and-tube waste-heat recovery configuration exposed to high-temperature thermal service and corrosive condensate chemistry. The governing flow, heat-transfer, species-transport and electrochemical equations are established models; the contribution of the work is their integrated use for material-performance screening under identical exchanger geometry and boundary conditions.

The base-case simulations predicted that SiC increased the average heat-transfer coefficient from 420 to $620\,\mathrm{W\,m^{-2}\,K^{-1}}$ and reduced pressure drop from 2.63 to $1.92\,\mathrm{Pa}$, giving a thermal-hydraulic performance factor of 1.64 relative to stainless steel. Electrochemical simulations also indicated lower localized current-density and corrosion-flux indicators

Table 8. Studied metrics for stainless steel and SiC.

Metric	Stainless steel	SiC	Relative change	Engineering meaning
Average heat-transfer coefficient, h ($\mathrm{W\,m^{-2}\,K^{-1}}$)	420	620	$+47.6\%$	Higher heat-transfer capacity under the same geometry and boundary conditions
Pressure drop, ΔP (Pa)	2.63	1.92	-27.0%	Lower hydraulic resistance in the base model
$h/\Delta P$ ($\mathrm{W\,m^{-2}\,K^{-1}\,Pa^{-1}}$)	159.7	322.9	$+102.2\%$	More heat-transfer coefficient per unit pressure loss
Thermal–hydraulic performance factor	1.00	1.64	$+64.0\%$	Combined heat-transfer and pressure-drop advantage
Corrosion current/flux indicator	Reference	Lower in base case	$> 60\%$ reduction reported as model indicator	Requires experimental electrochemical validation before absolute service-life prediction

for SiC than for stainless steel under the assumed chloride-, carbonate-, ammonium- and sulfur-bearing electrolyte. These trends support the technical promise of SiC for corrosive waste-heat recovery, but they should be interpreted as model-based comparative predictions rather than experimentally validated service-life data.

The study also identifies the limits of the present model. High-pressure ammonia compressibility, phase change, temperature-dependent properties, thermal-electrochemical feedback, passive-film breakdown/repassivation, plant-specific Nigerian condensate chemistry and mechanical/economic constraints were not fully resolved. Consequently, the framework is most appropriate for preliminary screening and hypothesis generation. Future work should combine COMSOL simulations with coupon-scale polarization/immersion testing, plant-condensate characterization, thermal-shock testing, pilot-scale validation and lifecycle-cost assessment before large-scale industrial adoption is recommended.

Data Availability Statement

Data will be made available on request.

Funding

This work was supported without any funding.

Conflicts of Interest

The authors declare no conflicts of interest.

AI Use Statement

The authors declare that no generative AI was used in the preparation of this manuscript.

Ethical Approval and Consent to Participate

Not applicable.

References

[1] Maghrabi, A. M., Song, J., & Markides, C. N. (2023). How can industrial heat decarbonisation be accelerated through energy efficiency?. *Applied Thermal Engineering, 233*, 121092. [CrossRef]

[2] Thiel, G. P., & Stark, A. K. (2021). To decarbonize industry, we must decarbonize heat. *Joule, 5*(3), 531-550. [CrossRef]

[3] Sundaramoorthy, S., Kamath, D., Nimbalkar, S., Price, C., Wenning, T., & Cresko, J. (2023). Energy efficiency as a foundational technology pillar for industrial decarbonization. *Sustainability, 15*(12), 9487. [CrossRef]

[4] Ononogbo, C., Nwosu, E. C., Nwakuba, N. R., Nwaji, G. N., Nwufo, O. C., Chukwuezie, O. C., ... & Anyanwu, E. E. (2023). Opportunities of waste heat recovery from various sources: Review of technologies and implementation. *Heliyon, 9*(2). [CrossRef]

[5] Castro Oliveira, M., Iten, M., Cruz, P. L., & Monteiro, H. (2020). Review on energy efficiency progresses, technologies and strategies in the ceramic sector focusing on waste heat recovery. *Energies, 13*(22), 6096. [CrossRef]

[6] Rajski, K., & Danielewicz, J. (2023). Heat transfer and heat recovery systems. *Energies, 16*(7), 3258. [CrossRef]

[7] Mondal, S., & De, S. (2026). An overview of waste heat recovery equipment and technologies: fundamentals and design aspects. *Waste Heat Recovery, Its Utilization and Performance Assessment*, 1-26. [CrossRef]

[8] Marzouk, S. A., Abou Al-Sood, M. M., El-Said, E. M., Younes, M. M., & El-Fakharany, M. K. (2023). A

comprehensive review of methods of heat transfer enhancement in shell and tube heat exchangers. *Journal of Thermal Analysis and Calorimetry, 148*(15), 7539-7578. [CrossRef]

[9] Saha, S., & Hasan, N. (2024). Numerical evaluation of thermohydraulic parameters for diverse configurations of shell-and-tube heat exchanger. *Results in Engineering, 23*, 102509. [CrossRef]

[10] Shah, R. K., Thonon, B. E. N. F. O. R. A. D. O., & Benforado, D. M. (2000). Opportunities for heat exchanger applications in environmental systems. *Applied Thermal Engineering, 20*(7), 631-650. [CrossRef]

[11] Qiao, J., Wang, Q., Na, E., Wen, X., Liang, Z., & Zhang, Y. (2025). RECENT PROGRESS IN WASTE HEAT RECOVERY TECHNOLOGY FOR BOILER FLUE GAS. *Therm. Sci, 29*(6), 4453-4471. [CrossRef]

[12] Khudhur, D. A., Tuan Abdullah, T. A., & Norazahar, N. (2022). A review of safety issues and risk assessment of industrial ammonia refrigeration system. *ACS Chemical Health & Safety, 29*(5), 394-404. [CrossRef]

[13] Jaafar, M. N., Rosli, M. I., Nordin, D., & Buhari, J. (2025). Systematic literature review on the risk assessment of ammonia refrigeration systems in the food industry. *Journal of Loss Prevention in the Process Industries, 96*, 105629. [CrossRef]

[14] Benzarti, Z., Arrousse, N., Serra, R., Cruz, S., Bastos, A., Tedim, J., ... & Carvalho, S. (2025). Copper corrosion mechanisms, influencing factors, and mitigation strategies for water circuits of heat exchangers: Critical review and current advances. *Corrosion Reviews, 43*(4), 429-455. [CrossRef]

[15] Ali, M., Ul-Hamid, A., Alhems, L. M., & Saeed, A. (2020). Review of common failures in heat exchangers–Part I: Mechanical and elevated temperature failures. *Engineering Failure Analysis, 109*, 104396. [CrossRef]

[16] Ali, M., Ul-Hamid, A., Khan, T., Bake, A., Butt, H., Bamidele, O. E., & Saeed, A. (2021). Corrosion-related failures in heat exchangers. *Corrosion Reviews, 39*(6), 519-546. [CrossRef]

[17] Fu, L., Liu, P., & Li, G. (2017). Numerical Investigation on the Low Temperature Corrosion Characteristics of Flue Gas Heat Exchanger. *Journal of Failure Analysis and Prevention, 17*(6), 1164-1173. [CrossRef]

[18] Panahi, H., Eslami, A., Golozar, M. A., & Laleh, A. A. (2020). An investigation on corrosion failure of a shell-and-tube heat exchanger in a natural gas treating plant. *Engineering Failure Analysis, 118*, 104918. [CrossRef]

[19] Isah, A., Sodiki, J. I., & Barinyima, N. (2019). Performance assessment of shell and tube heat exchangers in an ammonia plant. *European Journal of Engineering and Technology Research, 4*(3), 37-44. [CrossRef]

[20] Nicacio, J. A. P., Oliveira, F. C., & Dumont, M. R. (2024). Failure analysis and electrochemical testing of ammonium chloride corrosion in a heat exchanger in a diesel hydrotreating unit of a petroleum refinery. *Engineering Failure Analysis, 156*, 107758. [CrossRef]

[21] Francolle de Almeida, C., Saget, M., Delaplace, G., Jimenez, M., Fierro, V., & Celzard, A. (2023). Innovative fouling-resistant materials for industrial heat exchangers: a review. *Reviews in Chemical Engineering, 39*(1), 71-104. [CrossRef]

[22] Al Assaf, A. H., Ahmed, A., Mahaftha, D. M., Amhamed, A. I., Alrebei, O. F., & Jarrah, B. A. (2024). NH 3-H 2-Working Fluid-based Shell and Tube Heat Exchanger and the H 2 O-to-H 2 O Helical Heat Exchanger: A Novel Integration to Ammonia Production Plants. *Jordan Journal of Mechanical & Industrial Engineering, 18*(2). [CrossRef]

[23] Esabunor, T., Ikpeseni, S. C., Ekpu, M., Sada, S., & Orugba, H. O. (2025). Corrosion resistance of mild steel welded joints: Electrochemical analysis in five different environmental media. *Nigerian Journal of Technology, 44*(1), 29-38. [CrossRef]

[24] Estupiñán-Campos, J., Quitiaquez, W., Nieto-Londoño, C., & Quitiaquez, P. (2024). Numerical simulation of the heat transfer inside a shell and tube heat exchanger considering different variations in the geometric parameters of the design. *Energies, 17*(3), 691. [CrossRef]

[25] Treccani, L. (2023). Introduction to ceramic materials. *Surface-functionalized ceramics: for biotechnological and environmental applications*, 1-46. [CrossRef]

[26] Fend, T., Völker, W., Miebach, R., Smirnova, O., Gonsior, D., Schöllgen, D., & Rietbrock, P. (2011). Experimental investigation of compact silicon carbide heat exchangers for high temperatures. *International Journal of heat and mass transfer, 54*(19-20), 4175-4181. [CrossRef]

[27] Cramer, C. L., Lara-Curzio, E., Elliott, A. M., Aguirre, T. G., Yoon, B., Fricke, B. A., ... & Nawaz, K. (2024). Material selection and manufacturing for high-temperature heat exchangers: Review of state-of-the-art development, opportunities, and challenges. *International Journal of Ceramic Engineering & Science, 6*(5), e10230. [CrossRef]

[28] Pelanconi, M., Zavattoni, S., Cornolti, L., Puragliesi, R., Arrivabeni, E., Ferrari, L., ... & Ortona, A. (2021). Application of ceramic lattice structures to design compact, high temperature heat exchangers: material and architecture selection. *Materials, 14*(12), 3225. [CrossRef]

[29] Sommers, A., Wang, Q., Han, X., T'Joen, C., Park, Y., & Jacobi, A. (2010). Ceramics and ceramic matrix composites for heat exchangers in advanced thermal systems—A review. *Applied Thermal Engineering, 30*(11-12), 1277-1291. [CrossRef]

[30] Alfarawi, S. (2020). Evaluation of hydro-thermal shell-side performance in a shell-and-tube heat exchanger: CFD approach. *Journal of Advanced Research*

in Fluid Mechanics and Thermal Sciences, 66(1), 104-119. https://www.researchgate.net/publication/339527306

[31] Rahman, M. S. (2024). Computational fluid dynamics for predicting and controlling fluid flow in industrial equipment. *European Journal of Advances in Engineering and Technology, 11*(9), 1-9. https://www.researchgate.net/publication/384233737

[32] Łach, Ł., & Svyetlichnyy, D. (2025). Advances in numerical modeling for heat transfer and thermal management: a review of computational approaches and environmental impacts. *Energies, 18*(5), 1302. [CrossRef]

[33] Kiaghadi, M., Keshvarinia, M., & Sheikholeslami, M. (2025). Modeling, simulation, and artificial intelligence: a convergence in heat transfer systems. In *Revolutionizing Heat Transfer* (pp. 201-222). Elsevier. [CrossRef]

[34] Janoske, U., & Seifritz, S. (2024). Modelling of multi-species thin film flows based on the transport of ions including conjugate heat transfer applied to corrosion testing. *Progress in Computational Fluid Dynamics, an International Journal, 24*(5), 255-265. [CrossRef]

[35] Tang, S. Z., Wang, F. L., Ren, Q., & He, Y. L. (2017). Fouling characteristics analysis and morphology prediction of heat exchangers with a particulate fouling model considering deposition and removal mechanisms. *Fuel, 203*, 725-738. [CrossRef]

[36] Ben-Mansour, R., El-Ferik, S., Al-Naser, M., Qureshi, B. A., Eltoum, M. A. M., Abuelyamen, A., ... & Ben Mansour, R. (2023). Experimental/numerical investigation and prediction of fouling in multiphase flow heat exchangers: a review. *Energies, 16*(6), 2812. [CrossRef]

[37] Aslami, H., Nakisa, M., & Esmaeili, H. (2025). Investigating the effect of nanocoating on fouling in the plate heat exchanger: a computational fluid dynamics study. *Biofouling, 41*(10), 1023-1037. [CrossRef]

[38] Thekdi, A., Nimbalkar, S. U., Sundaramoorthy, S., Armstrong, K. O., Taylor, A., Gritton, J. E., ... & Cresko, J. (2021). *Technology assessment on low-temperature waste heat recovery in industry* (No. ORNL/TM-2021/2150). Oak Ridge National Laboratory (ORNL), Oak Ridge, TN (United States). [CrossRef]

[39] Kakaç, S., Liu, H., & Pramuanjaroenkij, A. (2002). *Heat exchangers: selection, rating, and thermal design*. CRC press. [CrossRef]

[40] Edreis, E., & Petrov, A. (2020, November). Types of heat exchangers in industry, their advantages and disadvantages, and the study of their parameters. In *IOP conference series: materials science and engineering* (Vol. 963, No. 1, p. 012027). IOP Publishing. [CrossRef]

[41] Zečević, N. (2021). *Advancement of process control system in ammonia production* (Doctoral dissertation, Sveučilište u Zagrebu, Sveučilište u Zagrebu Fakultet kemijskog inženjerstva i tehnologije). https://urn.nsk.hr/urn:nbn:hr:149:358922

[42] Zhang, J., Zhao, Y., Li, Y., & Zhang, F. (2021). Analysis of multiphase flow and heat and mass transfer for ammonium chloride crystallization of the high-pressure heat exchanger in hydrogenation unit. *Materials, 14*(24), 7754. [CrossRef]

[43] Sahin, K. B., Ozturk, M., Sahin, M., & Erdogdu, F. (2025). Computational analysis of single-shell-pass shell-and-tube heat exchangers with novel curved baffles and various tube layouts. *Innovative Food Science & Emerging Technologies*, 104243. [CrossRef]

[44] Thomas, J., Banda, M., Du, W., Yu, W., Chuang, A., France, D. M., & Singh, D. (2022). Development of a silicon carbide ceramic based counter-flow heat exchanger by binder jetting and liquid silicon infiltration for concentrating solar power. *Ceramics International, 48*(16), 22975-22984. [CrossRef]

[45] Yu, L., Hao, S., Nong, X., Cao, X., Zhang, C., Liu, Y., ... & Jiang, Y. (2021). Comparative Study on the Corrosion Resistance of 6061Al and SiC3D/6061Al Composite in a Chloride Environment. *Materials, 14*(24), 7730. [CrossRef]

[46] Lamm, B. W., Koyanagi, T., Lee, J. J., Keiser, J. R., Gietl, H., & Katoh, Y. (2025). Corrosion characteristics of silicon carbide fiber-reinforced composites in beryllium-bearing molten fluoride salt. *Corrosion Science, 244*, 112635. [CrossRef]

[47] ASTM International. (2020). *Standard specification for seamless carbon steel pipe for high-temperature service* (ASTM A106). ASTM International. https://store.astm.org/a0106_a0106m-19a.html

[48] Callister, W. D., Jr., & Rethwisch, D. G. (2020). *Materials Science and Engineering: An Introduction*. Wiley. [CrossRef]

[49] Shackelford, J. F. (1988). *Introduction to Materials Science for Engineers*. Internet Archive. https://arks.org/ark:/13960/t3dz88v7x

[50] Ezuber, H., & Zakir Hossain, S. M. (2023). A review of corrosion failures in shell and tube heat exchangers: roots and advanced counteractive. *Heat and Mass Transfer, 59*(6), 971-987. [CrossRef]

[51] Al-Mazeedi, H. A., Al-Wakaa, B., & Ravindranath, K. (2021). Window-type rupture of carbon steel pipe in a hydroprocessing plant of a petroleum refinery due to ammonium bisulfide corrosion. *Engineering Failure Analysis, 120*, 105089. [CrossRef]

[52] Speight, J. G. (2016). *Environmental Organic Chemistry for Engineers*. Butterworth-Heinemann.

[53] Zuo, W., Zhang, X., & Li, Y. (2020). Review of flue gas acid dew-point and related low temperature corrosion. *Journal of the Energy Institute, 93*(4), 1666-1677. [CrossRef]

[54] Mavi, A., & Chinyoka, T. (2023). Finite volume computational analysis of the heat transfer characteristic in a double-cylinder counter-flow

heat exchanger with viscoelastic fluids. *Defect and Diffusion Forum, 424*, 19–43. [CrossRef]

[55] Seddiq, M., Maerefat, M., & Mirzaei, M. (2014). Modeling of heat transfer at the fluid–solid interface by lattice Boltzmann method. *International Journal of Thermal Sciences, 75*, 28-35. [CrossRef]

[56] Lemmon, E. W., Bell, I. H., Huber, M. L., & McLinden, M. O. (2018). *NIST standard reference database 23: REFPROP, Version 10.0*. Gaithersburg: National Institute of Standards and Technology. https://www.nist.gov/srd/refprop

[57] Richerson, D. W., & Lee, W. E. (2018). *Modern ceramic engineering: properties, processing, and use in design*. CRC press. [CrossRef]

[58] Taylor, C. D. (2015). Corrosion informatics: an integrated approach to modelling corrosion. *Corrosion Engineering, Science and Technology, 50*(7), 490-508. [CrossRef]

[59] Castillo-Robles, J. M., de Freitas Martins, E., Ordejón, P., & Cole, I. (2024). Molecular modeling applied to corrosion inhibition: a critical review. *npj Materials Degradation, 8*(1), 72. [CrossRef]

[60] Illes, B., Medgyes, B., Dušek, K., Bušek, D., Skwarek, A., & Geczy, A. (2022). Numerical simulation of electrochemical migration of Cu based on the Nernst-Plank equation. *International Journal of Heat and Mass Transfer, 184*, 122268. [CrossRef]

[61] Uzdenova, A. M. (2024). Modeling of Ion Transport in a Three-Layer System with an Ion-Exchange Membrane Based on the Nernst–Planck and Displacement Current Equations. *Membranes and Membrane Technologies, 6*(1), 1-8. [CrossRef]

[62] Lewis, M. T., & Hickey, J. P. (2023). Conjugate heat transfer in high-speed external flows: A review. *Journal of Thermophysics and Heat Transfer, 37*(4), 697-712. [CrossRef]

[63] Xu, L. Y., & Cheng, Y. F. (2013). Development of a finite element model for simulation and prediction of mechanoelectrochemical effect of pipeline corrosion. *Corrosion Science, 73*, 150-160. [CrossRef]

[64] Jin, H. Z., Gu, Y., & Ou, G. F. (2021). Corrosion risk analysis of tube-and-shell heat exchangers and design of outlet temperature control system. *Petroleum Science, 18*(4), 1219-1229. [CrossRef]

[65] He, L., Wang, Y., Zhang, Q., Li, X., Xu, Y., & Huang, Y. (2023). Electrochemical study on the macro-cell corrosion of pipeline steel partially covered by different kinds of mineral deposits. *ACS omega, 8*(46), 44013-44029. [CrossRef]

[66] Sridhar, N. (2017). Local corrosion chemistry—a review. *Corrosion, 73*(1), 18–30. [CrossRef]

[67] Alexiadis, N., Fuchs, A., Troßmann, T., Bösing, I., Thöming, J., & La Mantia, F. (2025). Modeling and simulation of passive film formation and breakdown in chloride ion containing electrolytes–A Point Defect Model extension. *Corrosion Science, 256*, 113166. [CrossRef]

[68] Yang, J., Ma, L., Bock, J., Jacobi, A. M., & Liu, W. (2014). A comparison of four numerical modeling approaches for enhanced shell-and-tube heat exchangers with experimental validation. *Applied Thermal Engineering, 65*(1-2), 369-383. [CrossRef]

[69] Jaugstetter, M., Blanc, N., Kratz, M., & Tschulik, K. (2022). Electrochemistry under confinement. *Chemical Society Reviews, 51*(7), 2491-2543. [CrossRef]

[70] Mani, A., & Wang, K. M. (2020). Electroconvection near electrochemical interfaces: Experiments, modeling, and computation. *Annual review of fluid mechanics, 52*(1), 509-529. [CrossRef]

[71] Effiom, P. C., Effiom, S. O., Evareh, J. E., & Odu, P. O. (2024). Corrosion control in pipelines from carbon-II-oxide enhanced oil recovery (CO2–EOR). *Nigeria Journal of Engineering Research Unicross, 2*(2), 66-75. https://www.researchgate.net/publication/384256997

[72] Chen, D., Zhang, H., Zhao, G., Zhu, Z., Yang, J., He, J., ... & Zhu, Z. (2024). Investigating the corrosion resistance of different SiC crystal types: from energy sectors to advanced applications. *Langmuir, 40*(24), 12322-12342. [CrossRef]

[73] Gateman, S. M. (2020). *Investigating Corrosion of Simple and Complex Metallic Materials Using Macro and Micro Electrochemical Techniques*. McGill University (Canada). https://www.proquest.com/openview/75210a4596be5a25916668aa7fd21f9b/1

[74] Rahman, M. A. (2024). Enhancing reliability in shell and tube heat exchangers: establishing plugging criteria for tube wall loss and estimating remaining useful life. *Journal of Failure Analysis and Prevention, 24*(3), 1083-1095. [CrossRef]

[75] Newman, J., & Balsara, N. P. (2021). *Electrochemical systems*. John Wiley & Sons.

[76] Olsson, C. O., & Landolt, D. (2003). Passive films on stainless steels—chemistry, structure and growth. *Electrochimica acta, 48*(9), 1093-1104. [CrossRef]

[77] Gießgen, T., Mittelbach, A., Höche, D., Zheludkevich, M., & Kainer, K. U. (2019). Enhanced predictive corrosion modeling with implicit corrosion products. *Materials and Corrosion, 70*(12), 2247-2255. [CrossRef]

[78] Biscay, N., Henry, L., Adschiri, T., Yoshimura, M., & Aymonier, C. (2021). Behavior of silicon carbide materials under dry to hydrothermal conditions. *Nanomaterials, 11*(5), 1351. [CrossRef]

[79] Zhang, B., Wang, J., Wu, B., Guo, X. W., Wang, Y. J., Chen, D., ... & Ma, X. L. (2018). Unmasking chloride attack on the passive film of metals. *Nature communications, 9*(1), 2559. [CrossRef]

[80] Velukumar, V., Sekar, S. D., & Mothilal, T. (2026). CFD and experimental study of cyclone heat exchanger performance: NTU-effectiveness analysis. *Applied Thermal Engineering*, 129590. [CrossRef]

[81] Al-Haidari, S. R., & Al-Obaidi, A. R. (2025). Assessment improvement of heat performance and hydraulic thermal flow in a three-dimensional tube equipped with different turbulator corrugated arrangements. *Heat Transfer, 54*(4), 2594-2608. [CrossRef]

[82] Sun, X., Srinivasan, J., Kelly, R. G., & Duddu, R. (2021). Numerical investigation of critical electrochemical factors for pitting corrosion using a multi-species reactive transport model. *Corrosion Science, 179*, 109130. [CrossRef]

[83] Nešić, S. (2007). Key issues related to modelling of internal corrosion of oil and gas pipelines–A review. *Corrosion science, 49*(12), 4308-4338. [CrossRef]

[84] Hu, S. M., Wang, S. H., & Yang, Z. G. (2015). Failure analysis on unexpected wall thinning of heat-exchange tubes in ammonia evaporators. *Case Studies in Engineering Failure Analysis, 3*, 52-61. [CrossRef]

[85] Nesic, S., Postlethwaite, J., & Olsen, S. (1996). An electrochemical model for prediction of corrosion of mild steel in aqueous carbon dioxide solutions. *Corrosion, 52*(4), 280-294. [CrossRef]

[86] Bard, A. J., Faulkner, L. R., & White, H. S. (2022). *Electrochemical methods: fundamentals and applications*. John Wiley & Sons.

[87] Revie, R. W., & Uhlig, H. H. (2025). *Corrosion and corrosion control*. John Wiley & Sons.

[88] Hou, T. K., Kazi, S. N., Mahat, A. B., Teng, C. B., Al-Shamma'a, A., & Shaw, A. (2017). Industrial heat exchanger: operation and maintenance to minimize fouling and corrosion. *Heat Exchangers-Advanced Features and Applications, 1*(9), 193-207. [CrossRef]

[89] Song, C., Liu, Z., Babaei, M., Liu, R., & Hou, G. (2024). Mitigating low-temperature corrosion in flue-gas heat exchangers for improving thermal storage efficiency in geothermal power plants. *Thermal Science and Engineering Progress, 52*, 102673. [CrossRef]

[90] Laycock, N. J., & Newman, R. C. (1997). Localised dissolution kinetics, salt films and pitting potentials. *Corrosion science, 39*(10-11), 1771-1790. [CrossRef]

[91] Li, T., Wu, J., & Frankel, G. S. (2021). Localized corrosion: Passive film breakdown vs. Pit growth stability, Part VI: Pit dissolution kinetics of different alloys and a model for pitting and repassivation potentials. *Corrosion Science, 182*, 109277. [CrossRef]

[92] Strehblow, H. H., & Marcus, P. (1995). Mechanisms of pitting corrosion. *Corrosion mechanisms in theory and practice, 3*, 349-393. https://www.taylorfrancis.com/chapters/edit/10.1201/9780203909188-10

[93] Gaudet, G. T., Mo, W. T., Hatton, T. A., Tester, J. W., Tilly, J., Isaacs, H. S., & Newman, R. C. (1986). Mass transfer and electrochemical kinetic interactions in localized pitting corrosion. *AIChE journal, 32*(6), 949-958. [CrossRef]

[94] Frankel, G. S. (1998). Pitting corrosion of metals: a review of the critical factors. *Journal of the Electrochemical society, 145*(6), 2186-2198. [CrossRef]

[95] Linter, B. R., & Burstein, G. T. (1999). Reactions of pipeline steels in carbon dioxide solutions. *Corrosion science, 41*(1), 117-139. [CrossRef]

[96] Pistorius, P. C., & Burstein, G. T. (1992). Metastable pitting corrosion of stainless steel and the transition to stability. *Philosophical transactions of the royal society of London. Series A: Physical and Engineering Sciences, 341*(1662), 531-559. [CrossRef]